Surface & Coatings Technology 357 (2019) 669–683

Contents lists available at ScienceDirect

Surface & Coatings Technology

journal homepage: www.elsevier.com/locate/surfcoat

Surface functionalization via PEO coating and RGD peptide for nanostructured titanium implants and their in vitro assessment

Evgeny V. Parfenov[a,*], Lyudmila V. Parfenova[b], Grigory S. Dyakonov[c], Ksenia V. Danilko[d], Veta R. Mukaeva[a], Ruzil G. Farrakhov[a], Elena S. Lukina[b], Ruslan Z. Valiev[c]

[a] Department of Theoretical Basis of Electrical Engineering, Ufa State Aviation Technical University, 12 Karl Marx Street, Ufa 450008, Russia
[b] Institute of Petrochemistry and Catalysis of Russian Academy of Sciences, 141, Prospekt Oktyabrya, Ufa 450075, Russia
[c] Institute of Physics of Advanced Materials, Ufa State Aviation Technical University, 12 Karl Marx Street, Ufa 450008, Russia
[d] Bashkir State Medical University, 3 Lenin Street, Ufa 450000, Russia

ARTICLE INFO

Keywords:
Titanium implants
Nanostructured titanium
Plasma electrolytic oxidation
RGD peptide
In vitro tests
Fibroblasts

ABSTRACT

This research follows a biomimetic approach for implant surface design, and it concerns surface functionalization for nanostructured Ti Grade 4 with a composite coating obtained by plasma electrolytic oxidation (PEO) with organic pore filler of integrin-active RGD containing peptide (Arg-Gly-Asp-Cys). It was shown that Ti nanostructuring via ECAP-C technique almost two-fold improves its mechanical strength; also, the nanostructuring depassivates the surface, both PEO coated and uncoated. The PEO coating on nano-Ti contains 2–3% more biocompatible elements, amorphous and bio-crystalline phases. The RGD peptide was linked to the surface via phosphonate groups allowing the organic pore filler deposition by dipping method; the RGD presence in the PEO coating pores was proven by the EIS. For the in vitro tests, fibroblasts were used; it was shown that PEO coating on nano-Ti gives 43% increase in the number of cells compared to CG-Ti + PEO; the combination of PEO coating and RGD peptide on nano-Ti gives 45% increase in the number of cells compared to nano-Ti, and 66% compared to CG-Ti. Therefore, this surface functionalization contributes to the development of Ti implants having high strength and providing improved cell proliferation.

1. Introduction

Medical implants for osseosynthesis are the most demanded metal implants in traumatology; the majority of the fractures that require surgical intervention are treated by the installation of a plate or an intraosseous implant [1,2]. From the variety of available materials widely used in surgery, the most attractive choice is provided by using titanium and its alloys bioinert and highly corrosion resistant [3]. However, the absolute values of the strength for pure titanium are not quite high, and the titanium alloys having enough strength, e.g. Ti-6Al-4 V, contain harmful alloying components. This contradiction can be resolved by using advanced methods of severe plastic deformation (SPD) which helps to transform the material into the nanostructured state [4–6]. This increases the mechanical strength approximately twice due to the grain refinement; as current research shows, application of the nanostructured titanium with advanced mechanical properties opens the possibility to develop miniature medical devices of the new generation [7,8].

The cell adhesion, proliferation, and differentiation appear to be critically important for any medical device, but they significantly depend on physical and chemical properties of the metal implant surface [9]. Among the important surface properties that affect the vital activity of the cells, a large contribution is made by the surface roughness, morphology, contact angle, surface energy, the coating elemental and phase composition [10–15]. Therefore, it is extremely important to control the properties of the implant surface by deposition of biocompatible coatings obtained using various methods [16–18]. The coatings obtained by physical and chemical methods exhibit good adhesion, high surface area, and they have mechanical properties close to that of the human bone [19,20]; however, they show insufficient bioactivity due to their inorganic nature. The coatings with organic molecules, including oligopeptides, provide good osseointegration, prevent fibrous tissue formation, but they have low adhesion which can result in implantation failure [21,22].

As it was recently shown, with the application of plasma electrolytic oxidation (PEO), the formation of coatings having unique morphology becomes possible [23–25]. The coatings obtained by PEO, not only possess excellent adhesion, but also include Ca- and P- containing

* Corresponding author.
E-mail address: evparfenov@mail.ru (E.V. Parfenov).

https://doi.org/10.1016/j.surfcoat.2018.10.068
Received 13 February 2018; Received in revised form 23 October 2018; Accepted 24 October 2018
Available online 25 October 2018
0257-8972/

Table 1
PEO coating regime.

Mode	Regulation	Positive pulse		Negative pulse		Frequency (Hz)	Temperature (°C)	Duration (min.)
		Voltage (V)	Duty cycle (%)	Voltage (V)	Duty cycle (%)			
Pulsed bipolar	Voltage	470	51	40	26	300	20	10

phases, and provide high surface area formed by their porous structure [26–28]. Various reports promise improvement in osseointegration after formation of the PEO coatings by using in vitro and in vivo techniques [29–33]. However, the information regarding PEO coatings application on ultrafine grained and nanostructured titanium is limited; though, improvement of mechanical, corrosion and blood compatibility properties have been reported [34–36].

Another approach for improving osseointegration uses biologically active coatings based on RGD (arginine-glycine-aspartic acid), a tripeptide fragment, which is an integral part of many proteins of the intercellular matrix, and to which the cells attach using specific receptors on their surface – integrins [37]. High adhesion of such organic molecules to the implant surface can be provided by introducing phosphonate groups which have a high affinity for metal ions [38], and a great ability to bind to the oxidized titanium surface [39]. Such bifunctional molecules based on ε-caproic acid bisphosphonate and RGD were used elsewhere to modify titanium metal surface [40]. However, a relatively smooth metal surface cannot provide a long retention time for such molecules; as a result, this surface modification method may cause the problems in the device performance in vivo.

Recently proposed biomimetic or bioinspired approach to the implant design concerns imitation of the bone structure and properties at all levels – mechanical, physical, chemical and biological [41–43]. The nanostructured Ti can provide appropriate mechanical characteristics, the PEO coating can imitate physical and chemical properties of the bone, and RGD pore filler can stimulate an appropriate biological response of such implant. The researchers consider bioactive organic pore fillers for the PEO coatings; this includes polytetrafluoroethylene for non-fouling coatings [44], chitosan for improved biocompatibility [45], gentamicin-PLGA for antibacterial ability [46], silver particles containing for fungicidal properties [47]. However, no information is available concerning RGD-modified PEO coatings, especially on nanostructured Ti substrate.

Therefore, the aim of the research is to uncover the effect of titanium nanostructuring, PEO coating and RGD pore fillers on the surface properties, and cell viability and proliferation, in order to contribute to the development of a new implant generation with advanced surface properties.

2. Experimental

2.1. Titanium mechanical properties and nanostructuring

Titanium Grade 4 (ASTM F67) was chosen as the substrate material in this research. The impurity content (wt%) for Ti Grade 4 is: Fe – 0.15, C – 0.05, O – 0.36, N – 0.007; H – 0.002, Ti – balance. Mechanical tensile tests were carried out in accordance to ASTM E8-13a at room temperature with the initial strain rate of $10^{-3}\,s^{-1}$ using an INSTRON-type testing machine. Cylindrical samples with a gauge length of 15 mm and a diameter of 3 mm were assessed. Ambient temperature stress-controlled fatigue tests of nanostructured and as supplied titanium were performed at a load ratio $R(s_{min}/s_{max}) = -1$ and rotational bending loading scheme with a frequency of 50 Hz in accordance with ASTM-E466. For every type of the structure, in accordance with ASTM E8-13a, three identical samples were tested.

Titanium nanostructuring was performed using Conform type of an equal channel angular pressing (ECAP-C) with consequent drawing [48]. As a result of the severe plastic deformation, nanostructured titanium rods having a diameter of 6 mm and a length of 3 m were obtained. The samples for the microstructure characterization and further surface modifications were cut from one rod (denoted as nano-Ti). Coarse-grained (CG-Ti) samples were also cut from the same size Ti Grade 4 rod.

2.2. PEO coating

Rectangular coupons cut from the CG-Ti and nano-Ti rods (20 × 5 mm, thickness 1 mm, surface finish Ra ≤ 0.15 μm) were used for the PEO. A hole, 2.5 mm in diameter, was made near the top of the sample in order to attach a screw holder. During the PEO, the samples were immersed into the electrolyte to the depth of 50–70 mm from the electrolyte level. The electrolyzer was a 10-l glass tank with a stainless steel cooling coil arranged into a cubic form 20 × 20 × 20 cm in size and served as a cathode. The aqueous electrolyte (pH = 11.5) contained 20 g/l $Na_3PO_4{\cdot}12\ H_2O$ and 25 g/l $Ca(CH_3COO)_2$; the electrolyte volume was 4 l. The treatment time was 10 min. All the experiments were carried out at the same temperature of 20 °C maintained with ± 1 °C accuracy by a heating and cooling systems operated under TRM202 (OWEN, Russia) microcontroller regulation. The electrolyte was stirred by aeration in order to maintain the same temperature over the volume and to prevent sedimentation of calcium phosphates formed in this cloudy electrolyte.

The PEO process was used in pulsed bipolar mode under voltage regulation with the regime shown in Table 1. As follows from the previous work, these process parameters provide good adhesion and biocompatible phase content for PEO coatings on commercially pure Ti [23]. A modular DC power supply (12 modules MeanWell SPV-1500-48 for positive supply and 4 modules for negative supply) providing up to +600/–200 V and up to 30 A was used; it supplied a regulated voltage to a half bridge inverter SKM400GB12T4 providing bipolar output voltage pulses. The whole setup has a PC based control system.

2.3. Synthesis of RGD- functionalized derivatives

The following reagents were used: MSA (Methanesulfonic acid, 98%), PCl_3 (98%), β-alanine (97%), all purchased from Acros Organics. EMCS (N-[ε-maleimidocaproyloxy]succinimide ester, 97%, Thermo Fisher Scientific) and oligopeptide RGDC (Arg-Gly-Asp-Cys, trifluoroacetate salt, Bachem) were used.

The ^{1}H, ^{13}C, and ^{31}P NMR spectra were recorded on a Bruker AVANCE-500 spectrometer (500.17 MHz (^{1}H), 125.78 MHz (^{13}C), and 202.46 MHz (^{31}P)). 1D and 2D NMR spectra (COSY HH, HSQC, HMBC, NOESY) were recorded using standard Bruker pulse sequences. As the solvents and the internal standards, $CDCl_3$ and D_2O were employed. IR spectra were recorded on vacuum spectrometer Bruker VERTEX-70v. Mass spectra were obtained on spectrometer MALDI-TOF/TOF Autoflex III (Bruker) using 2,5-dihydroxybenzoic acid (2,5-DHB) or α-cyano-4-hydroxycinnamic acid (CHCA) as matrixes.

2.3.1. Synthesis of aminoethylphosphonic acid (1)

Compound **1** was prepared from β-alanine by a modified procedure [49]. A 50 ml flask equipped with a magnetic stirrer was loaded with β-alanine (0.89 g, 10 mmol) and 4.5 ml of methanesulfonic acid. Then, 2.8 ml (32 mmol) of PCl_3 was added dropwise in 5 min, and the

contents of the flask were stirred at 80–85 °C for 4 h. After cooling the mixture to r.t., 5 ml of water was added, and the mixture was stirred further at 105 °C for 2 h. The pH was adjusted to 6 by adding 5 ml of 50 wt% aqueous sodium hydroxide to the mixture. Then, the mixture was stirred for 1 h and the precipitate was removed by filtration. The crude product was dissolved in 5 ml of water with heating at 70 °C; upon cooling, the solid phase was filtered off. The precipitate was washed with 5 ml of methanol. Yield 80% (2.0 g). IR (ν, cm^{-1}): 3448, 1613 (OH); 1526, 916 (NH_2); 1377, 1171 (P = O); 2726, 2675, 1281 (CH_2). ^{1}H NMR (D_2O) δ: 2.22 (t, J = 8 Hz, 2H, C^2H_2); 3.27 (t, J = 8 Hz, 2H, C^3H_2). ^{13}C NMR (D_2O) δ: 72.5 (t, $^1J_{C\text{-}P}$ = 134 Hz, C^1), 30.1 (C^2); 36.00 (C^3). ^{31}P NMR (D_2O) δ: 17.03. MALDI-TOF/TOF m/z 234.018 $[M\text{-}H]^+$, calc. for $C_3H_{10}NO_7P_2$ 235.069.

2.3.2. Synthesis of 4-N-(6-maleimidohexanoyl)aminoethane-1-hydroxy-1,1-bisphosphonic acid (2)

According to [50], β-alaninebiphosphonate **1** (9.12 mg, 0.039 mmol) was dissolved in 0.6 ml of water, the pH of the solution was adjusted to 8–9 using 0.1 N NaOH (~180 μl). An equimolar amount of the EMCS linker (12.00 mg, 0.039 mmol) dissolved in 0.2 ml of 1,4-dioxane was added to the stirring solution. The reaction mixture was stirred at room temperature for 15–30 min, then neutralized to pH = 7 with 0.1 N HCl and concentrated under reduced pressure. Compound **2** was obtained in quantitative yield as a white powder. ^{1}H NMR (D_2O) δ: 1.13–1.24 (m, 2H, C^7H_2); 1.43–1.57 (m, 4H, C^6H_2, C^8H_2); 1.98–2.13 (m, 2H, C^2H_2); 2.14 (t, J = 7.4 Hz, 2H, C^5H_2); 3.35–3.44 (m, 2H, C^3H_2); 3.42 (t, J = 7.0 Hz, 2H, C^9H_2); 6.75 (d, J = 4.2 Hz, 2H, HC = CH). ^{13}C NMR (D_2O) δ: 24.81 (C^6); 25.41 (C^7); 27.28 (C^8); 32.76 (C^2); 35.49 (C^3); 35.74 (C^5); 37.43 (C^9); 72.93 (C^1); 134.27 (C^{11}); 173.42 (C^{10}); 176.46 (C^4); ^{31}P NMR (D_2O) δ: 17.74. MALDI-TOF/TOF m/z 428.086 $[M]^+$; calc. for $C_{13}H_{22}N_2O_{10}P_2$ 428.269.

2.3.3. Synthesis of RGDC-4-N-(6-maleimidohexanoyl)aminoethane-1-hydroxy-1,1-bisphosphonic acid (3)

According to [50], 5 mg of RGDC was dissolved in 1.45 ml of bi-distilled water, the pH was adjusted to 7 by addition of 0.1 N NaOH (~120 μl). An equivalent amount of compound **2** was added to the solution. The reaction mixture was stirred for 1–2 h at 38–40 °C until a pinkish-violet shade appeared, and then the solvent was removed under reduced pressure. Compound **3** was obtained in quantitative yield as a pink-white powder. IR (ν, cm^{-1}): 3400 (OH); 1377, 1142 (P = O); 2400 (CH_2). ^{1}H NMR (D_2O) δ: 1.13–1.29 (m, 2H, C^7H_2); 1.39–1.56 (m, 4H, C^6H_2, C^8H_2); 1.56–1.69 (m, 2H, $C^{26}H_2$); 1.81–1.89 (m, 2H, $C^{25}H_2$); 1.97–2.12 (m, 2H, C^2H_2); 2.14 (t, J = 7.5 Hz, 2H, C^5H_2); 2.48–2.71 (m, 2H, $C^{19}H_2$); 3.10–3.21 (m, 2H, $C^{27}H_2$); 3.12–3.28 (m, 2H, $C^{14}H_2$), 3.35–3.44 (m, 2H, C^3H_2); 3.42 (t, J = 7.2 Hz, 2H, C^9H_2); 3.83–3.93 (m, 1H, $C^{24}H$); 3.83–3.94 and 3.98–4.07 (both m, 2H, $C^{22}H_2$); (m, 1H, $C^{22}H_2$); 4.31–4.44 (m, 1H, $C^{15}H$); 4.55–4.66 (m, 1H, $C^{18}H$). ^{13}C NMR (D_2O) δ: 23.59 (C^{26}); 24.85 (C^6); 25.48 (C^7); 26.33 (C^8); 28.80 (C^{25}); 33.04 (C^2); 33.41 (C^{14}); 35.74 (C^5); 35.89 (C^3); 38.20 (C^{19}); 38.93 (C^9); 40.45 (C^{27}); 42.41 (C^{22}); 51.41 (C^{18}); 53.06 (C^{24}); 54.35 (C^{15}); 72.70 (C^1); 156.75 (C^{28}); 170.73 (C^{21},C^{23}); 172.62 (C^{17}); 175.81 (C^{16}); 176.34 (C^4); 177.95 (C^{10},C^{13},C^{20}). ^{31}P NMR (D_2O) δ: 17.92. MALDI-TOF/TOF m/z 877.629 $[M]^+$; calc. for $C_{28}H_{49}N_9O_{17}P_2S$ 877.751.

2.4. Material and surface characterization

The CG titanium macrostructure was studied using Olympus GX51 optical microscope. For optical metallography, the sample surface was polished mechanically and etched in a chemical solution consisting of hydrofluoric acid – 20 vol%, nitric acid – 20 vol%, and distilled water – 60 vol%. The substrate microstructure was studied using a scanning electron microscope (SEM) JEOL JSM-6490LV and a JEM-2100 transmission electron microscope (TEM) at accelerating voltages of 10 kV and 200 kV respectively. The samples for TEM studies were cut out by electric discharge machining. After mechanical thinning down to 100 μm, the samples were subjected to electrochemical polishing using Tenupol-5system. The electropolishing was conducted using chemical solution consisting of perchloric acid – 5 vol%, butanol – 35 vol%, and methanol – 60 vol%. The coating surface morphology was analyzed with the scanning electron microscope JEOL JEM-6390 for in-plane and cross-section views.

In order to assess the substrate structure and to evaluate the coating porosity, the SEM and TEM images were processed using ImageJ software and in accordance with ASTM E112-10. By adjusting threshold in the grayscale images, the relative surface area taken by the objects of interest being darker than the neighboring places was calculated by the program. In order to evaluate the pore size distribution, Analyze Particles algorithm was used. To get a statistically reliable result, at least 20 images for every measurement were used.

The surface roughness R_a was measured by a profilometer TR-220 using the track length of 0.25 mm and the ranges 0–0.1, 0–0.3 and 0–1 μm with 5% accuracy of the range. Ten measurements were taken on each side of the sample and averaged. The elemental analysis of the coatings was evaluated with Shimadzu EDX-800P spectrometer. The phase composition of the surface layer was characterized by X-ray diffractometer Rugaku Ultima IV in Cu Kα radiation at 40 kV and 40 mA using 0.02°. step scan with 2 s exposure, from 20 to 80° 2θ. Further, the XRD spectra were processed using Philips X'PertHighscore Plus software with PDF2 pattern database.

In order to evaluate the fraction of amorphous constituent in the PEO coating, Keller and Dollase method was used [23,51]. The XRD spectra of Ca-, P- containing coatings generally exhibit a wide peak between 24 and 37° 2θ corresponding to amorphous calcium phosphates. This peak was approximated as a background using 1st and 3rd order polynomials. The spectrum area above the 1st order background was treated as 100%; the area between the 1st and 3rd order backgrounds was treated as belonging to the amorphous constituent; the rest was treated as belonging to the crystalline constituent. Further, the crystalline constituent of the coating was analyzed using a normalized reference intensity ratio (RIR) method employed in the Semiquant procedure of Philips X'PertHighscore Plus software [52].

The electrochemical tests were carried out in Ringer's solution (0.86 wt% NaCl, 0.03 wt% KCl, 0.033 wt% $CaCl_2$, pH 7.4) at temperature 37.0 ± 0.2°C using P-5X (Elins, Russia) electrochemical system. After the open circuit potential (OCP) was settled within ± 20 mV for at least 30 min, the electrochemical impedance spectroscopy (EIS) was performed from 100 kHz to 1 mHz with the magnitude of 10 mV around the OCP. The potentiodynamic polarization (PDP) test was run from −350 mV to +350 mV with respect to the settled OCP at a rate of 0.25 mV/s. The reference electrode was silver chloride electrode filled with 3.5 M KCl. The counter electrode was a platinum rod.

The PDP results were processed using Tafel analysis [52]. For the PDP curves having linear Tafel regions at ± 200 mV overpotentials, both anodic and cathodic slopes were used; for those having only cathodic linear Tafel regions, only cathodic slopes were used. The corrosion current i_{corr} was evaluated at the intersection of cathodic and anodic (if available) tangent lines with the level of E_{corr}. The polarization resistance R_p was evaluated as a slope of the polarization curve at ± 10 mV overpotentials for all the samples [53]. The EIS results were analyzed using ZView software from Scribner Associates [54].

Three samples of each type were analyzed, and the corresponding surface properties were averaged.

2.5. In vitro assessment

Following other studies of fibroblasts on Ti implant surface [55–58], we have chosen them as a model to study the cell viability and proliferation because biomaterials should not cause destruction not only to the bone tissue but also to adjacent soft tissues, such as cartilage and tendon. Since fibroblasts are the main cellular constituent of the soft tissue, a study on proliferation, morphology, and adhesion of the

fibroblasts on differently modified titanium surfaces shall provide an important indication of the surface cytocompatibility and suitability for further possible implant applications [59].

The coated and uncoated Ti samples were ultrasonically cleaned for 10 min in 95% ethanol and finally washed with deionized water, dried on air and sterilized by autoclaving at 134 °C. This temperature does not affect the Ti nanostructure and the PEO coating. Four types of samples were tested: CG-Ti, nano-Ti, CG-Ti + PEO, nano-Ti + PEO. In order to deposit the organic pore filler, nano-Ti + PEO samples were put into a Petri dish with 10^{-3} M solution of the RGD-derivative, sterilized by filtration with CA 0.22 μm filter. In 3 h the samples were dried on the air in a laminar box. Afterward, all the samples were put into a plastic 24-well tissue culture plate.

Human embryonic lung fibroblasts (FLECH-104) purchased from BIOLOT (Russia) were cultured in Dulbecco's modified Eagle's medium (DMEM) (Sigma) containing 10% fetal bovine serum (FBS) (SPL Life Sciences), in 25-cm^2 culture flasks (SPL Life Sciences) in a humidified 5% CO_2 atmosphere. The medium was changed twice a week. After reaching a monolayer, the cells were detached using trypsin/Versene solution 1:1 (BIOLOT) and counted using automated cell counter TC20 (BioRad).

The trypsinized FLECH-104 suspension was placed into each well of the plate with the samples (0.8 ml containing $16{\cdot}10^3$ cells). The cells in the wells having no samples were treated as a control. The culture plates were incubated during 1 and 7 days in the standard conditions (37 °C, 5 vol% CO_2). The culture plate itself (polystyrene) was used as a negative control (NC).

The cell proliferation was determined by EZ4U assay (Biomedica), a modification of the MTT test, which evaluates the cell metabolic activity that is proportional to the number of the adherent cells. Three samples of each type were transferred after the incubation into another 24-well plate with 0.8 ml of fresh DMEM medium. Then 80 μl of the activated EZ4U solution was added to every well and incubated at 37 °C, 5 vol% CO_2 for 3.5 h. Optical absorbance was measured using microplate reader (Spark10M, Tecan) at 450 nm with a reference wavelength of 620 nm. The optical density per mm^2 was calculated as.

$$\text{Optical density with respect to NC (\%)} = \frac{(a - a_{blank})/s}{(A - a_{blank})/S} \cdot 100\% \quad (1)$$

where a – absorbance of the test sample at 450 nm minus absorbance at 620 nm;A – absorbance of the negative control sample at 450 nm minus absorbance at 620 nm;a_{blank} – absorbance of the blank solution of DMEM with no cells at 450 nm and at 620 nm;s – surface area of the test sample;S – surface area of the NC well.

The adherent cells were also assessed through fluorescence microscopy on one sample of each type with cytochemical stains: DAPI (4,6-diamidino-2-phenylindole) for nuclei. After the incubation, the fibroblasts attached to the surface of the samples were fixed with 70 vol% ethanol, stained with DAPI (0.1 mg/ml), and examined in reversed phase fluorescence with a Zeiss Axiovert D1 microscope, using a filter at 340/360 nm.

The mean value and the standard deviation for three measurements of the optical density were calculated with respect to the negative control. One-way ANOVA test with Tukey multiple comparisons was used to compare the means among the groups. GraphPad Prism 6.01 was used for calculation, and statistical significance levels were set at $p < 0.05$.

3. Results and discussion

3.1. Ti nanostructuring

Titanium microstructure in the initial state is shown in Fig. 1a; the average grain size of the as-received material is 25 μm. The CG-Ti has mechanical properties shown in Table 2.

After ECAP-C and consequent drawing, as a result of the severe plastic deformation, the average grain size decreased to 0.1 μm (Fig. 1b, c). Derived from the TEM image analysis both for the transverse and longitudinal sections of the rod, the grain size distributions follow normal distribution law, and they exhibit peaks at 80 nm (Fig. 2a). Although some grains after SPD reach the size of 200–300 nm which at the first glance is higher than that accepted for nanostructured materials [60], within the grains there are various nanostructured features having size under 100 nm: nanotwins, dislocation substructures, segregations and precipitations that are important microstructural elements and produce influence on the material properties. The nano-Ti rod drawing leads to some elongation of the grains into the longitudinal direction (Fig. 1c); as a result, axial type of the structure dominated by a strong <1 0 $\bar{1}$ 0> fiber was formed. This is supported by a pole figure shown in Fig. 2b. Therefore, the SPD significantly changes the material structure, increases the densities of grain boundaries and defects. As shown elsewhere [48], the increase in the strength of nano-Ti compared to CG-Ti is achieved due to mechanisms of substructure strengthening and grain-boundary strengthening.

Results of mechanical tests show that the nanostructuring increased the mechanical properties more than twice compared to CG-Ti (Table 2), but Young's modulus for CG-Ti and nano-Ti is the same $E \approx 112$ GPa [61]. Moreover, the mechanical properties of nano-Ti samples appear to be much higher compared to results of other grain refinement techniques described elsewhere [62]. Therefore, Ti nanostructuring via ECAP-C + drawing can act as an advanced option for implant applications instead of Ti-6Al-4 V alloy having mechanical properties better than that for CG-Ti Grade 4, but having alloying elements harmful to a human body [3].

3.2. Differences in PEO coatings for CG and nanostructured Ti substrates

Fig. 3 presents SEM images of the top view and cross-section of the PEO coating for CG-Ti and nano-Ti substrates. Table 3 shows values of the surface properties before and after the plasma electrolytic oxidation. The coating has a typical microstructure exhibiting pores with an average size of 3 μm providing the opportunities for the cells to attach to the surface with protein pseudopodia. The coating cross-section is typical for the PEO layers; the coating has large pore openings and a network of thin pore channels resulting from the microdischarge propagation through the oxide layer.

For the CG-Ti, the coating appears to be slightly thicker; however, the standard deviation is quite large so that there is no statistical difference between the coating thickness for CG-Ti + PEO and nano-Ti + PEO. However, the SEM cross-section image for the nano-Ti + PEO coating shows a much finer inner structure of the pores. Since the microdischarges during the PEO process end on electric field concentrators like micro profile peaks, grain boundaries, and impurities, for the nanostructured substrate, much even distribution of these objects can also refine the microdischarge streamer, thus, resulting in a finer structure of the coating [63]. In addition, the surface roughness appears to be slightly smaller for the PEO coating on the nanostructured substrate due to this effect.

The average pore size has a negligible difference between the surface types. Nevertheless, the porosity is slightly higher for the nanostructured substrate; this can be explained by the pore size distribution (Fig. 4). The PEO coating on the nanostructured substrate shows larger pores up to 13–14 μm in diameter; some of them can be seen in Fig. 3d in cross-section.

Table 4 presents the elemental content resulting from EDX analysis, and Fig. 5 shows typical XRD patterns of the substrates and PEO coatings on CG-Ti and nano-Ti. Both methods confirm the presence of biocompatible elements and compounds within the surface layer. Taking into account the standard deviations of the elemental content, nano-Ti + PEO coatings have 2.5% larger content of biocompatible elements and lower Ti content than CG-Ti + PEO (Fig. 6a, b).

The XRD spectra for the substrate follow typical Ti pattern;

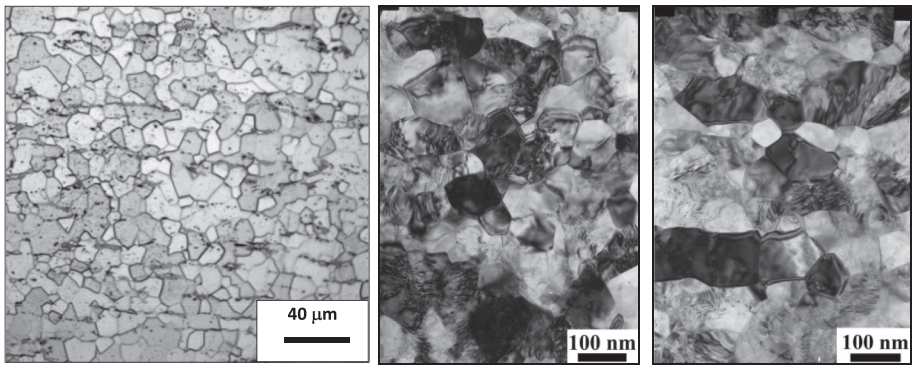

Fig. 1. Microstructure of Ti Grade 4: (a) as received CG-Ti (optical microscopy); (b) nano-Ti, transverse section (TEM); (c) nano-Ti, longitudinal section (TEM).

Table 2
Mechanical properties of CG-Ti and nano-Ti samples.

Material structure	Ultimate tensile strength (MPa)	Yield strength (MPa)	Elongation (%)	Reduction area (%)	Fatigue strength at 10^7 cycles (MPa)
CG-Ti (as received)	700 ± 20	530 ± 15	25 ± 3	52 ± 4	340
Nano-Ti (ECAP-C + drawing)	1330 ± 25	1267 ± 20	11 ± 2	48 ± 3	620

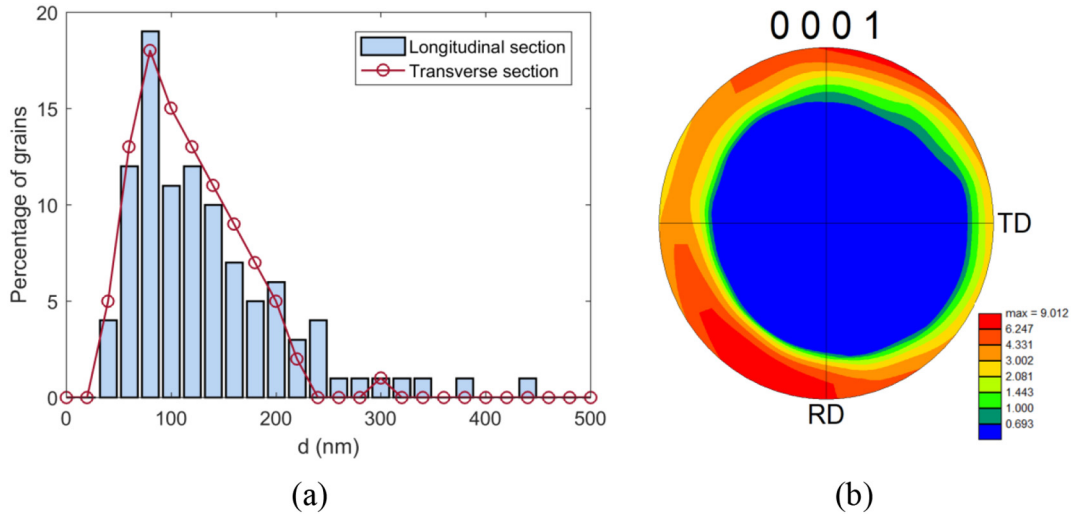

Fig. 2. Grain size distributions for longitudinal and transverse sections of nano-Ti obtained via TEM image analysis (a) and pole figure (0001) for a transverse section of the nano-Ti rod (b).

however, for the nano-Ti, the peaks show some broadening, which is typical for nanostructured materials. The spectra of the PEO coatings contain peaks belonging to the Ti substrate, rutile and anatase TiO_2 modifications, perovskite $CaTiO_3$, hydroxyapatite $Ca_{10}(PO_4)_6(OH)_2$ and β-tricalcium phosphate $Ca_3(PO_4)_2$. Similar to other studies, the XRD pattern exhibits a broad peak between 20 and 40° 2θ coming from amorphous calcium phosphate compounds which are beneficial for bone regeneration in implant applications [17].

The phase compositions of the PEO coatings are shown in Table 5. As follows from the analysis, the amount of the amorphous phases reaches 70%; for the nano-Ti + PEO its content is higher (Fig. 6c, d). The total crystalline content of 29–32% primarily belongs to rutile; for nano-Ti + PEO its content is lower than that for CG-Ti + PEO by 3.8%. Also, for nano-Ti + PEO, the amount of perovskite is larger by 3%. Considering the standard deviations, the amount of hydroxyapatite, tricalcium phosphate, and anatase in the PEO coatings appears to be the same for both substrates.

Comparison of the results shows that the PEO coating on the nano-Ti substrate contains more biocompatible elements and amorphous and crystalline phases; therefore, it appears to be more promising for implant applications.

3.3. Synthesis of the bifunctional molecule with RGD motif

The PEO coating in combination with an organic biologically active phosphonic acid derivative containing a tripeptide RGD fragment was used to stimulate the cell adhesion. It was assumed that the oxidized metal surface with a developed pore network would ensure better adhesion of organic molecules. In order to link the RGD-peptide to the PEO coating, we synthesized amino acid bisphosphonate (**1**) by a reaction of β-alanine with PCl_3 in methanesulfonic acid according to a procedure described elsewhere [49]. It was found that the reaction carried out at an elevated temperature (85–90 °C) for 4–5 h provides the product yield of 80%. The introduction of the tripeptide proceeds through activation of the aminophosphonate with *N*-succinimidyl-6-maleimidocaproate, followed by conjugation with the SH-group of the cysteine residue (C) of the linear RGDC sequence in an aqueous neutral medium [40] (Fig. 7).

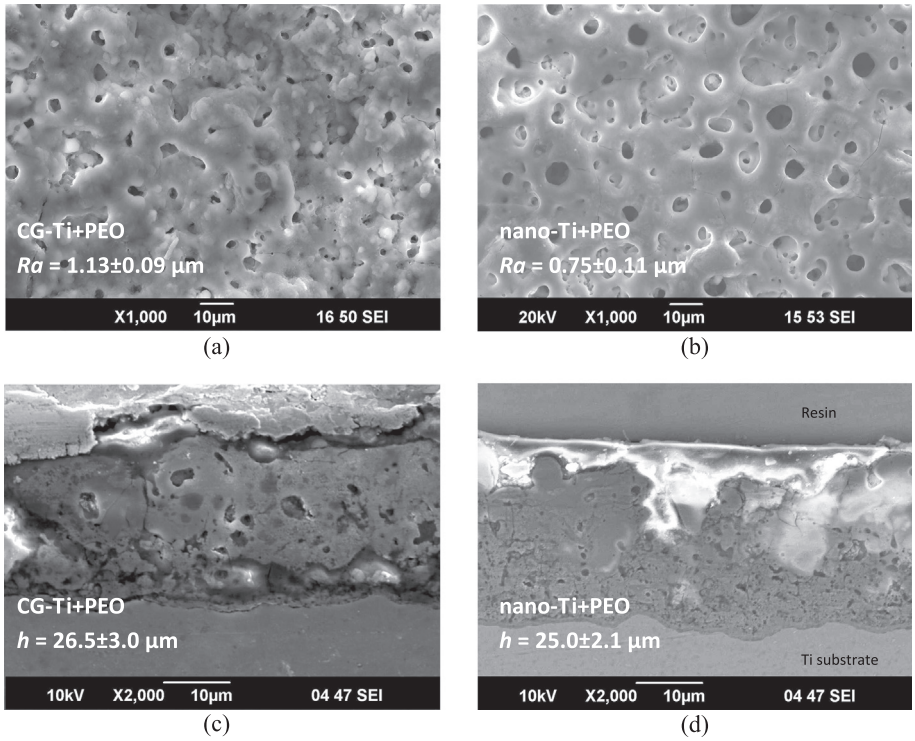

Fig. 3. PEO coating morphology for coarse-grained and nanostructured Ti substrates with an indication of the coating thickness *h* and roughness *Ra*: (a) CG-Ti + PEO, top view; (b) nano-Ti + PEO, top view; (c) CG-Ti + PEO, cross-section; (d) nano-Ti + PEO, cross-section.

Table 3
Surface properties of uncoated and PEO coated coarse grained and nanostructured Ti samples.

Sample type	Ra (µm)	h (µm)	Porosity (%)	Average pore size (µm)
CG-Ti	0.13 ± 0.10	–	–	–
Nano-Ti	0.14 ± 0.10	–	–	–
CG-Ti + PEO	1.13 ± 0.09	26.5 ± 3.0	8.8 ± 0.5	3.3 ± 0.6
Nano-Ti + PEO	0.75 ± 0.11	25.0 ± 2.1	10.2 ± 0.5	3.1 ± 0.6

The structure of the resulting RGD-derivative **3** was proved by the means of NMR, IR and mass spectrometry MALDI TOF/TOF. The ^{1}H NMR spectrum shows the signals that correspond to the aminophosphonate moiety, the linker fragment, and RGDC. The reaction between compound **2** and RGDC is evidenced by the absence of the double bond proton signal at the δ_H 6.75 ppm in the ^{1}H NMR spectrum. The ^{31}P NMR spectrum contains a single resonance line at δ_P 17.96 ppm attributed to phosphonate groups. Mass spectrometry MALDI TOF/TOF of compound **3** exhibits peak with *m/z* 877.629 corresponding to the molecule weight.

3.4. Electrochemical behavior of CG and nanostructured Ti substrates with PEO and RGD treatments

PDP test (Fig. 8) shows significant differences in the corrosion potential E_{corr} between the coated and uncoated, CG and nano, RGD modified and non-modified surfaces (Table 6).

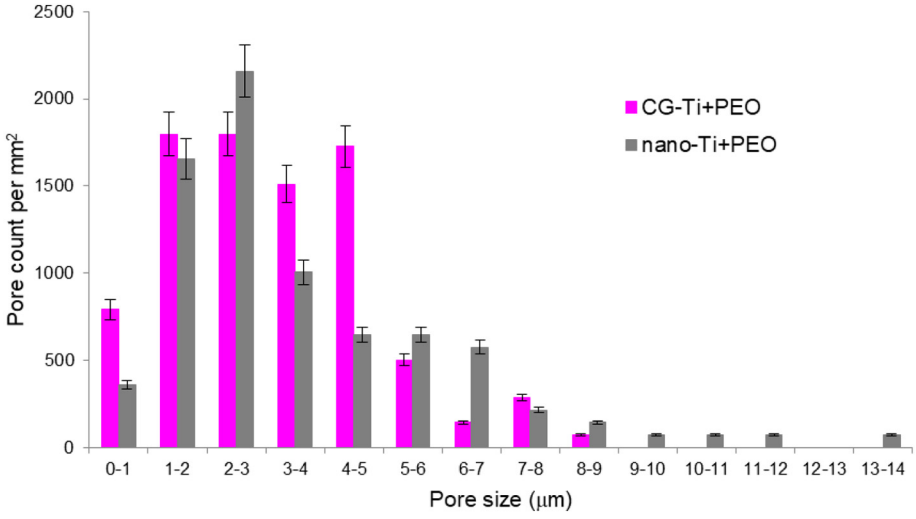

Fig. 4. Pore size distribution for PEO coatings on coarse-grained and nanostructured Ti substrates.

Table 4
EDX analysis results for elemental content of the substrates and PEO coatings on CG-Ti and nano-Ti.

Elements (wt%)	Ti	Ca	P	Na	Fe	others
CG-Ti	99.2 ± 0.1	–	–	–	0.2 ± 0.1	0.6 ± 0.1
Nano-Ti	99.4 ± 0.1	–	–	–	0.2 ± 0.1	0.4 ± 0.1
CG-Ti + PEO	68.2 ± 0.4	21.4 ± 0.5	7.5 ± 0.1	2.1 ± 0.1	0.1 ± 0.01	0.7 ± 0.1
Nano-Ti + PEO	65.6 ± 1.0	22.6 ± 0.8	8.3 ± 0.2	2.4 ± 0.5	0.1 ± 0.01	1.0 ± 0.04

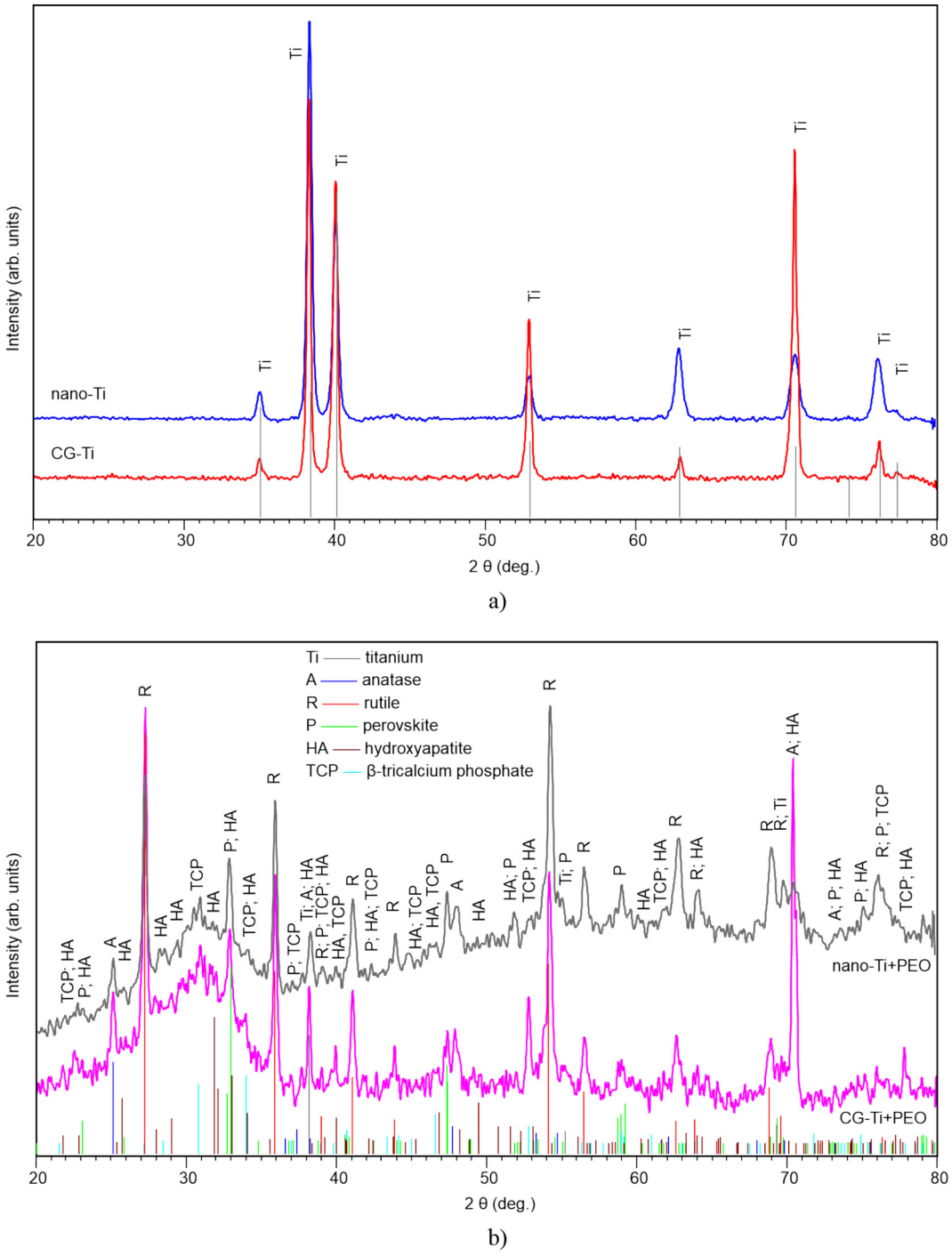

Fig. 5. X-ray diffraction patterns of CG-Ti and nano-Ti substrates (a) and corresponding PEO coatings (b).

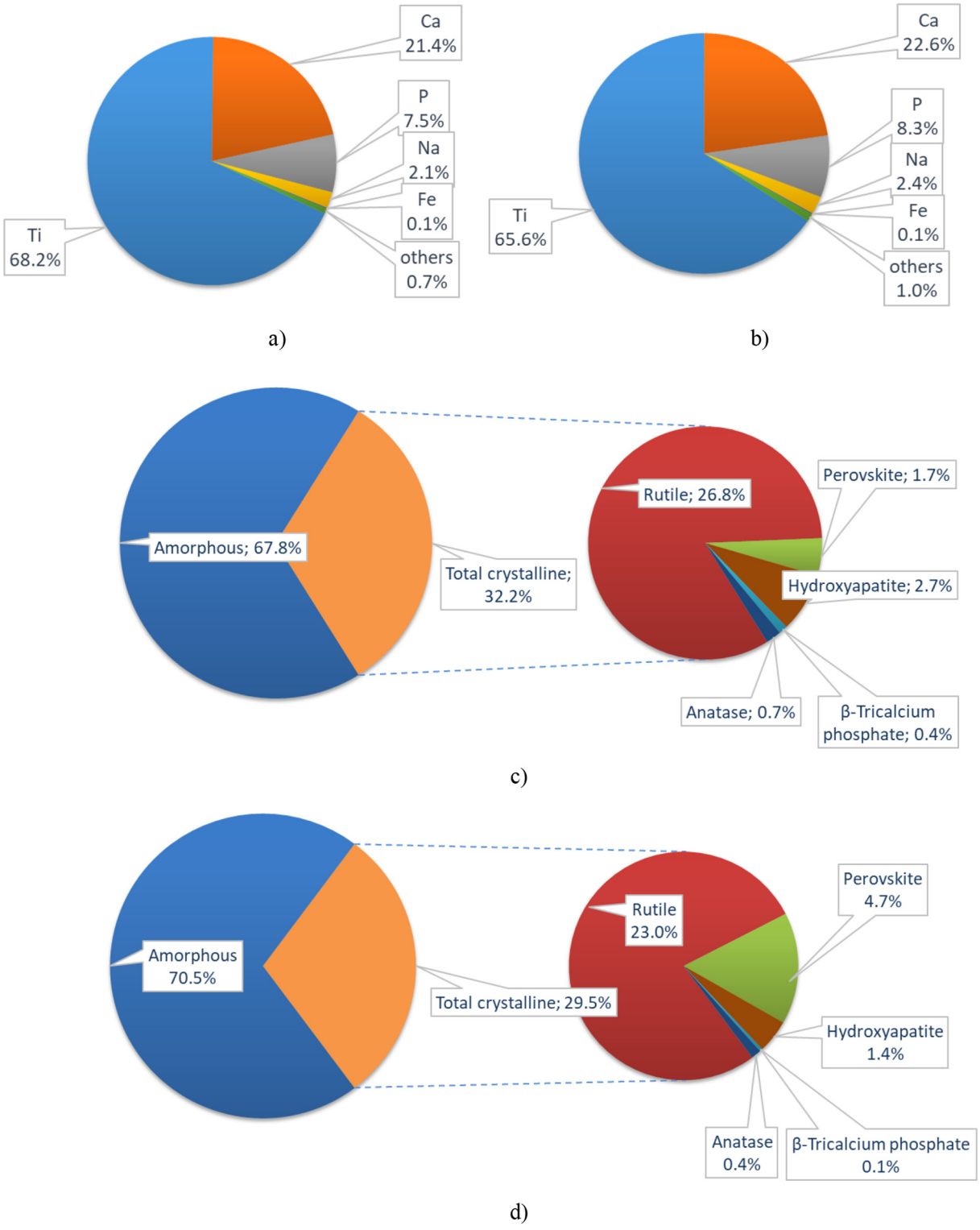

Fig. 6. Elemental (a, b) and phase (c, d) compositions of PEO coatings on CG-Ti (a, c) and nano-Ti (b, d) substrates.

With the Ti nanostructuring, the substrate depassivates, since the E_{corr} becomes more negative. This is consistent with other findings showing the same trend of the E_{corr} values [64]. A significant increase in the volume fraction of grain boundaries and triple junctions provide higher energies than the bulk of the material; therefore, nano-Ti becomes more chemically active; also, a higher density of the grain boundaries increases the surface reactivity through the increase of the electron activity and diffusion [65]. The i_{corr} values slightly decrease from CG-Ti to nano-Ti; this type of the behavior is attributed to the changes in the surface area taken by cathode (the bulk of the grain) and anode (grain boundaries). When decreasing the grain size, the cathode area cannot counter the increasing grain boundary as the anode site; this results in suppression of the cathode reaction: i_{corr} and E_{corr} simultaneously decrease [66].

Application of the PEO coating passivates the surface; as a result, the PDP curves have tips at higher potentials E_{corr}; the dependency on

Table 5
Phase composition relative mass fractions (wt%) obtained from semi-quantitative analysis of XRD patterns for PEO coatings on CG-Ti and nano-Ti substrates.

Compound name	Chemical formula	CG-Ti + PEO	Nano-Ti + PEO
Amorphous	–	67.8 ± 6.1	70.5 ± 4.7
Crystalline, including:	–	32.2 ± 5.9	29.5 ± 3.8
Rutile	TiO_2	26.8 ± 2.3	23.0 ± 1.8
Perovskite	$Ca(TiO_3)$	1.7 ± 1.2	4.7 ± 1.1
Hydroxyapatite	$Ca_5(PO_4)_3(OH)$	2.7 ± 1.4	1.4 ± 0.8
β-Tricalcium phosphate	$Ca_3(PO_4)_2$	0.4 ± 0.3	0.1 ± 0.03
Anatase	TiO_2	0.7 ± 0.6	0.4 ± 0.1

the substrate grain size remains the same: CG-Ti + PEO has more passive surface than nano-Ti + PEO due to the effect described above. With the PEO coating formation, the corrosion currents increase compared to the uncoated substrate; this can be explained by the coating composition discussed in p. 3.2. Since the coating contains not only passive titania, but also electrochemically active Ca and Na species, the corrosion current increases compared to the substrate itself and titania-only PEO coatings obtained elsewhere [67].

Introducing of the RGD into the PEO coating even more depassivates the surface, and the resulting E_{corr} is lower than that for the uncoated substrate. The corrosion current i_{corr} increase at least by an order of magnitude. This indicates that the RGD appears to be attached to the PEO coated substrate. The influence of the nanostructured substrate is still in effect: CG-Ti + PEO + RGD has more passive surface than nano-Ti + PEO + RGD, but the corrosion current i_{corr} is almost the same; this indicates that the RGD motifs contribute to the increase in the corrosion currents. The polarization resistance R_p (Table 6) appears to be the highest for the uncoated samples; this can be explained by the fact that in the case of the uncoated Ti, a naturally formed thin uniform oxide layer protects the surface; this layer has very few defects; therefore, it has the highest polarization resistance. Application of the Ca-, P- containing PEO coating not only increases the corrosion current as discussed above but also decreases the polarization resistance; RGD containing PEO coatings have the lowest values of the R_p.

All the coated samples exhibit passivation regions in the PDP curves: instead of a positive anodic Tafel slope, the current density saturates at a certain value denoted as a passivation current i_{pass} (Table 6). The passivation current generally follows the same pattern as the corrosion current i_{corr} does; introducing RGD motifs increases the passivation current. As shown elsewhere, the biocompatible coatings should contain some calcium phosphates that should gradually dissolve in the extracellular matrix providing the material for the bone growth and calcification [17]. Therefore, unlike pure titania PEO coatings, the biocompatible coatings can show higher corrosion and passivation currents than the substrate. From the calcium phosphates, hydroxyapatite is the less soluble compound, thus, it constitutes the crystalline phase of the bone [68]. Also, it is the amorphous phase of calcium phosphates which is beneficial for bone reconstruction. The higher the crystallinity of the hydroxyapatite appears to be, the less impact it gives to the coating bioactivity [69]; this holds for the nano-Ti + PEO coating compared to CG-Ti + PEO.

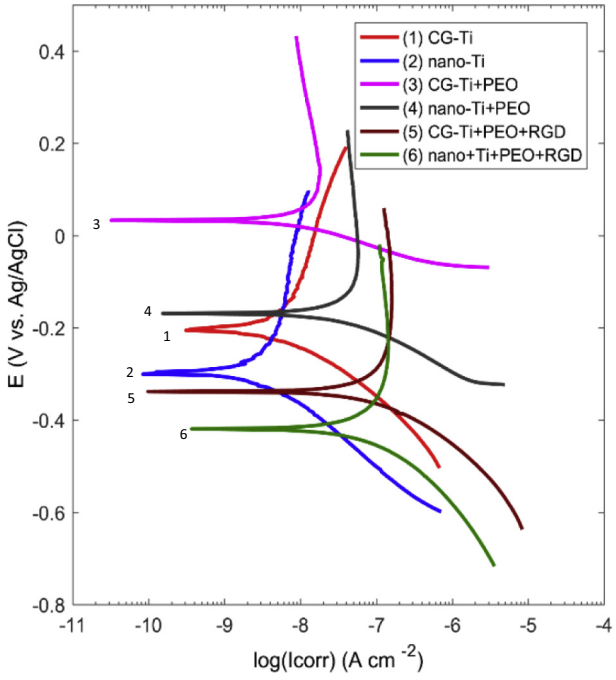

Fig. 8. Potentiodynamic polarization test results for CG and nanostructured Ti substrates, uncoated, PEO coated and RGD modified.

The electrochemical impedance spectroscopy results are shown in Fig. 9 as complex and Bode plots of the frequency response. The complex plots have almost linearly increasing parts at the lowest frequencies indicating either Warburg or constant phase element (CPE) presence. The coated samples have a part of a semi-circle indicating a presence of a charge transfer resistance in parallel with a double layer capacitance which impurity is usually represented with a CPE having impedance $Z_{CPE} = \frac{1}{(j\omega)^n \cdot Q}$ [54]. Consequently, the uncoated CG-Ti and nano-Ti impedance spectra can be fitted with a Randles equivalent circuit shown in Fig. 10a [54]. More complex Randles circuit includes

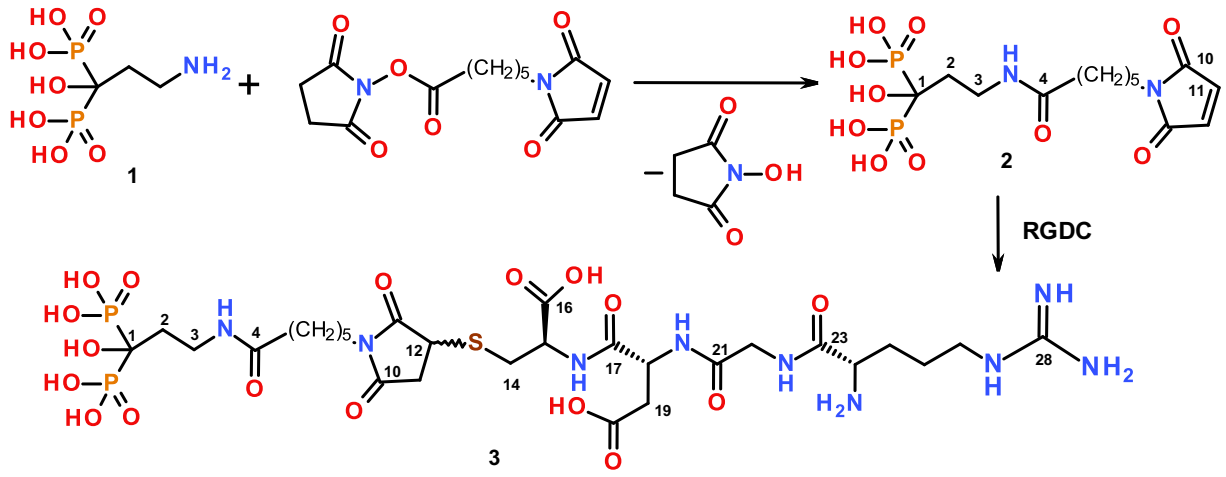

Fig. 7. Scheme of RGD-derivative **3** synthesis.

Table 6
Corrosion potential E_{corr}, corrosion current i_{corr}, polarization resistance R_p and passivation current i_{pass} in Ringer's solution for CG and nanostructured Ti substrates, uncoated, PEO coated and RGD modified.

Sample type	CG-Ti	nano-Ti	CG-Ti + PEO	nano-Ti + PEO	CG-Ti + PEO + RGD	nano-Ti + PEO + RGD
E_{corr} (V vs. Ag/AgCl)	−0.206 ± 0.025	−0.301 ± 0.024	0.033 ± 0.029	−0.169 ± 0.022	−0.338 ± 0.031	−0.419 ± 0.026
i_{corr} (A·cm^{-2})	$5.9{\cdot}10^{-9}$ ± $2.1{\cdot}10^{-9}$	$4.3{\cdot}10^{-9}$ ± $0.6{\cdot}10^{-9}$	$7.7{\cdot}10^{-9}$ ± $1.2{\cdot}10^{-9}$	$35.1{\cdot}10^{-9}$ ± $2.2{\cdot}10^{-9}$	$176{\cdot}10^{-9}$ ± $32.1{\cdot}10^{-9}$	$168{\cdot}10^{-9}$ ± $49.1{\cdot}10^{-9}$
R_p (Ω·cm^2)	$77.5{\cdot}10^5$ ± $32.7{\cdot}10^5$	$103{\cdot}10^5$ ± $14.4{\cdot}10^5$	$17.9{\cdot}10^5$ ± $2.32{\cdot}10^5$	$6.72{\cdot}10^5$ ± $0.34{\cdot}10^5$	$3.43{\cdot}10^5$ ± $0.22{\cdot}10^5$	$4.46{\cdot}10^5$ ± $0.24{\cdot}10^5$
i_{pass} (A·cm^{-2})	–	–	$6.49{\cdot}10^{-9}$ ± $0.21{\cdot}10^{-9}$	$35.6{\cdot}10^{-9}$ ± $0.76{\cdot}10^{-9}$	$112{\cdot}10^{-9}$ ± $13.1{\cdot}10^{-9}$	$91.4{\cdot}10^{-9}$ ± $5.04{\cdot}10^{-9}$

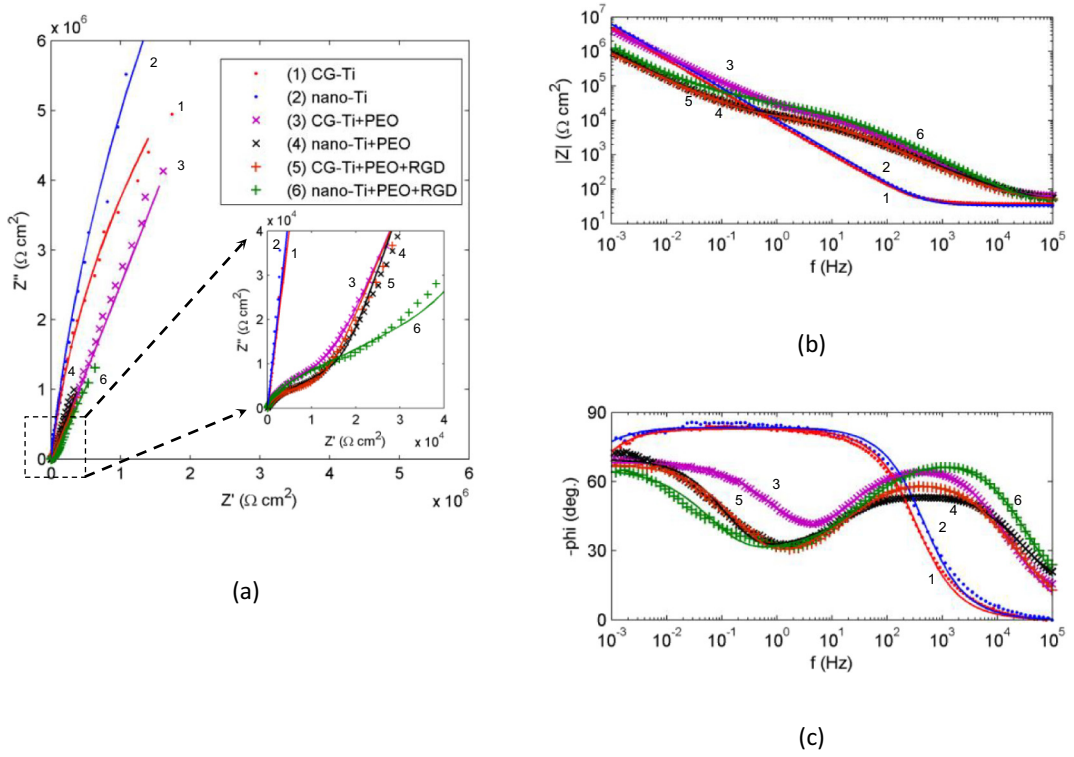

Fig. 9. EIS results for CG and nanostructured Ti substrates, uncoated, PEO coated and RGD modified: (a) complex plot; (b) Bode plot for the impedance modulus; (c) Bode plot for the phase angle.

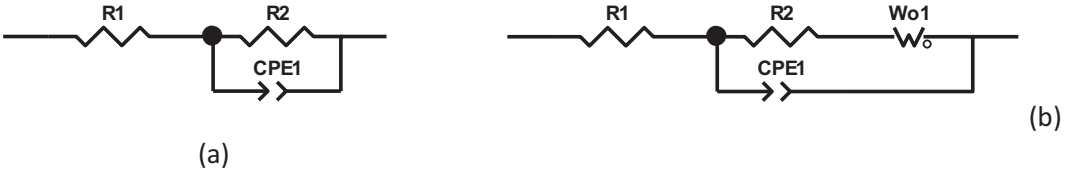

Fig. 10. Equivalent circuits used for the impedance spectra fitting for CG and nanostructured Ti substrates: (a) uncoated; (b) PEO coated.

Warburg impedance $Z_{Wo} = R{\bullet}\frac{ctnh[(j\omega T)^P]}{(j\omega T)^P}$ standing for diffusion processes in the coating pores (Fig. 10b); this circuit can be used to describe the EIS results of all the coated samples. The diffusion process usually appears as the growth of the complex plot at 45° (ideally) with the frequency decrease [70]. These equivalent circuits are consistent with those discussed elsewhere for a similar system [71]. One semicircle stands for the R2-CPE pair; its influence at the lowest frequencies is negligible compared to the Warburg impedance growing with the frequency decrease. The fit results are presented in Table 7. The values of χ^2 and parameter estimation errors are sufficiently small to consider the fits to be appropriate.

Compared to R_2 and *Wo-R*, the electrolyte resistance R_1 appears to be quite small, averaging to 42.1 ± 4.7 Ω. The charge transfer resistance R_2 has much higher values for the uncoated substrates than that for the coated ones; considering its close relation to the polarization resistance R_p, both resistances follow the same trend with the surface treatment. The *CPE-Q* parameter for the uncoated samples is an order of magnitude higher than that of the coated ones; consequently, the natural oxide layer is thinner than the PEO coating and very uniform due to *CPE-n* value very close to unity. With such values, the complex plot for CG-Ti and nano-Ti is just a part of a large semi-circle with a diameter equal to R_2. For the coated substrates we can see a half of this semi-circle in the complex plot. R_2 values are lower for RGD modified surface; this indicates that the organic layer became incorporated into the PEO coating pores, and it increased the chemical activity of the surface. This is consistent with the PDP results. For the coated substrates the *CPE-n* values are lower than that for the uncoated substrate because the porosity penetrates the oxide layer and introduces

Table 7
Equivalent circuit fit results for EIS of CG and nanostructured Ti substrates, uncoated, PEO coated and RGD modified.

Sample type	CG-Ti	Nano-Ti	CG-Ti + PEO	Nano-Ti + PEO	CG-Ti + PEO + RGD	Nano-Ti + PEO + RGD
R_2 (Ω cm^2)	$2.78{\cdot}10^{7} \pm 2.34{\cdot}10^{6}$	$5.77{\cdot}10^{7} \pm 1.10{\cdot}10^{7}$	12,597 ± 552	9105 ± 314	7687 ± 292	8761 ± 439
CPE-Q (μF s^{n-1} cm^{-2})	$2.16{\cdot}10^{-5} \pm 7.37{\cdot}10^{-8}$	$1.71{\cdot}10^{-5} \pm 8.33{\cdot}10^{-8}$	$2.14{\cdot}10^{-6} \pm 3.25{\cdot}10^{-8}$	$6.70{\cdot}10^{-6} \pm 1.38{\cdot}10^{-7}$	$4.65{\cdot}10^{-6} \pm 1.08{\cdot}10^{-7}$	$1.26{\cdot}10^{-6} \pm 3.81{\cdot}10^{-8}$
CPE-n	0.92 ± 0.001	0.93 ± 0.001	0.78 ± 0.002	0.67 ± 0.002	0.72 ± 0.002	0.80 ± 0.003
Wo-R (Ω cm^2)	–	–	21,332 ± 1586	33,393 ± 1098	20668 ± 1085	93895 ± 2931
Wo-T (s)	–	–	0.12 ± 0.01	1.75 ± 0.08	0.95 ± 0.07	4.48 ± 0.24
Wo-P	–	–	0.38 ± 0.0005	0.41 ± 0.0014	0.38 ± 0.0014	0.36 ± 0.0023
χ^2 ($\times 10^{-3}$)	8.4	12.5	0.2	0.5	1.2	1.8

more conductive current density (*CPE-n* → 0) in addition to the displacement current density (*CPE-n* → 1). For the nano-Ti + PEO coating, the *CPE-n* value is lower than that for the CG-Ti + PEO; this is consistent with larger porosity (Fig. 3) and results obtained elsewhere [35].

The diffusion process parameters described by Warburg element show that the impedance *Wo-R* increases for the nano-Ti substrate for all the coatings; moreover, the time constant *Wo-T* also increases. This can be supported by the coating cross-section morphology showing finer pore mesh for this substrate (Fig. 3). The surface modification with RGD also increases these parameters, especially for the nano-Ti substrate, thus, showing the influence of both of the substrate nanostructuring and RGD introduction.

3.5. *In vitro test results supporting the efficiency of proposed functionalization*

The results of the fibroblast viability and proliferation after one and seven days are shown in Fig. 11. As follows from the figure, for the first day the number of adsorbed cells on the PEO coating is smaller compared to the uncoated substrate. This effect is particularly pronounced in the case of the nanostructured substrate. After 7 days, a significant increase in the number of cells can be seen on the surface of all the samples compared to NC. For CG-Ti and CG-Ti + PEO, the number of the cells appears to be statistically equal. However, the effect of Ti nanostructuring appears for all the samples, and the fibroblast viability increases from CG-Ti to nano-Ti, then to nano-Ti + PEO, and to nano-Ti + PEO + RGD. Consequently, the growth of fibroblasts is much faster for the PEO coated nanostructured titanium. As a result, the combination of PEO coating containing and RGD motifs give nearly 45% increase in the number of cells compared to nano-Ti, and 66% compared to CG-Ti and CG-Ti + PEO.

This effect is illustrated in Figs. 12 and 13 showing fluorescence microscope images of the samples. The analysis of the PEO coatings shows more Ca and P elemental content, more amorphous phase and more biocrystalline phase (perovskite, hydroxyapatite, tricalcium phosphate) contents on the nano-Ti substrate than that on CG-Ti (Tables 4, 5). The increase in this content on the nanostructured substrate can improve the cell proliferation [33,72,73], along with a decrease in roughness and growth of porosity. Moreover, for nano-Ti + PEO surface the number of pores with size 2–3 μm is higher than that for CG-Ti + PEO; also, 9–14 μm pits appear in the surface; probably, this can contribute to more favorable conditions for the cell attachment and growth.

The increase in the coating resistance R_2 + *Wo-R* (Table 7) from nano-Ti to nano-Ti + PEO, and to nano-Ti + PEO + RGD decreases the charge transfer effect for the Ti ion release. CG + PEO coating has thicker porosity channels; the RGD introduction does not affect the diffusion so that *Wo-R* does not statistically change. For the nano-Ti + PEO, the RGD introduction hampers the diffusion since both *Wo-T* and *Wo-R* increase; probably, the RGD blocks the thin porosity channels acting as organic brushes on the pore walls. As a result, less contaminated with Ti ions environment can also stimulate cell growth. In the literature, a similar effect was described for the influence of roughness [56,58,74] and pore size obtained of PEO coatings [75] on adhesion and cell growth. Moreover, the known positive effect of RGD deposited on the titanium on the cell adhesion and proliferation [76–78] now can be extended onto PEO coatings.

Finally, the nanostructuring of the Ti substrate material in combination with the inorganic PEO and organic integrin-active RGD coating supports cell survival and promotes their growth.

4. Conclusions

This research shows that mechanical, physical, chemical and biological properties of titanium implants can be significantly improved due to a system effect gained from the application of the following

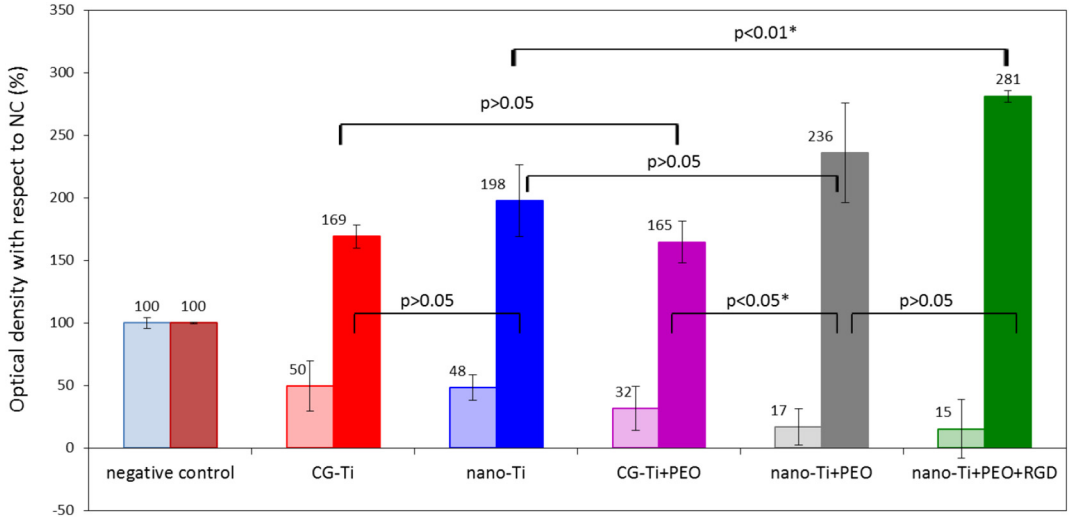

Fig. 11. Optical density showing viability and proliferation of fibroblasts cultured on the surface of CG and nanostructured Ti substrates, uncoated, PEO coated and RGD modified samples after 1 and 7 days (left and right bars respectively).

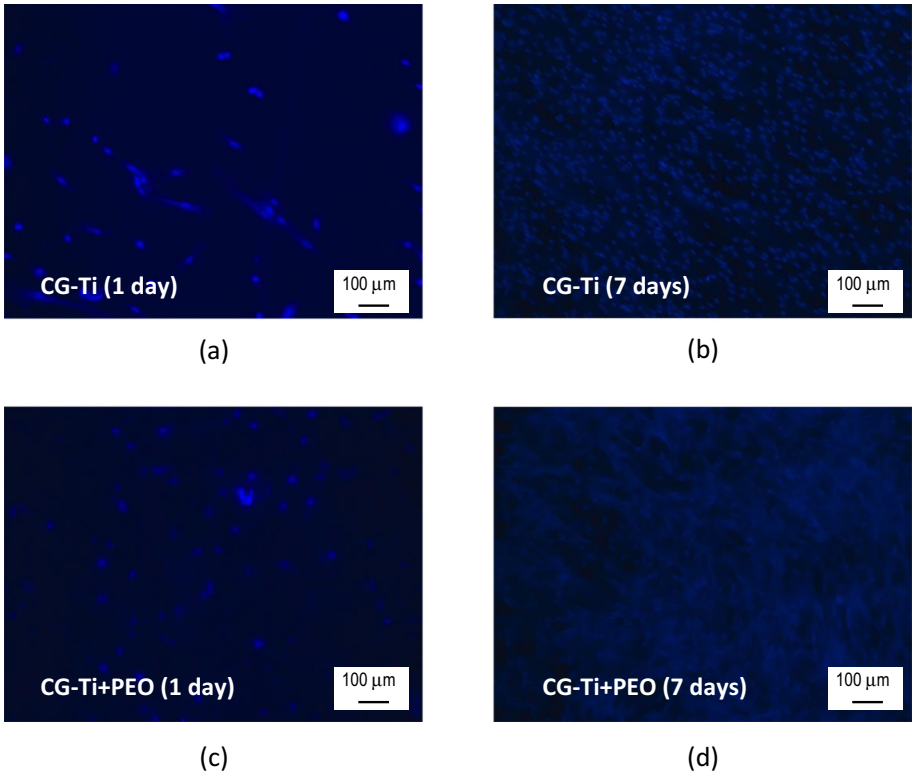

Fig. 12. Fluorescence microscope images of fibroblast cell nuclei after proliferation test for the coarse-grained Ti samples: (a) CG-Ti, 1 day; (b) CG-Ti, 7 days; (c) CG-Ti + PEO, 1 day; (d) CG-Ti + PEO, 7 days.

techniques:

(1). Titanium nanostructuring via the ECAP-C method which increases almost two-fold the material strength, so that CP Ti Grade 4 can have mechanical strength comparable to that of Ti-6Al-4 V alloy, but the material would not have harmful alloying elements such as Al and V.
(2). Plasma electrolytic oxidation helps to form a porous inorganic coating having good adhesion to the Ti substrate and containing Ca-, P- compounds beneficial to a bone regeneration; for the nanostructured Ti substrate, the pore mesh is much finer than that for the coarse-grained substrate, also, the surface appears to be less passive electrochemically, and it contains 2–3% more biocompatible elements, amorphous and bio-crystalline phases.
(3). RGD integrin-active oligopeptide can be introduced into the PEO coating pores using bisphosphonate linkers allowing its deposition by dipping; after RGD modification, the PEO coated surface depassivates, but the coating diffusion resistance and time constants increase, especially for the nano-Ti substrate compared to CG-Ti.

The application of these techniques provides an increase in the cell viability and proliferation for the nanostructured substrate compared to coarse-grained Ti so that every step: nanostructuring, PEO coating and RGD modification increase the number of the cells adsorbed on the

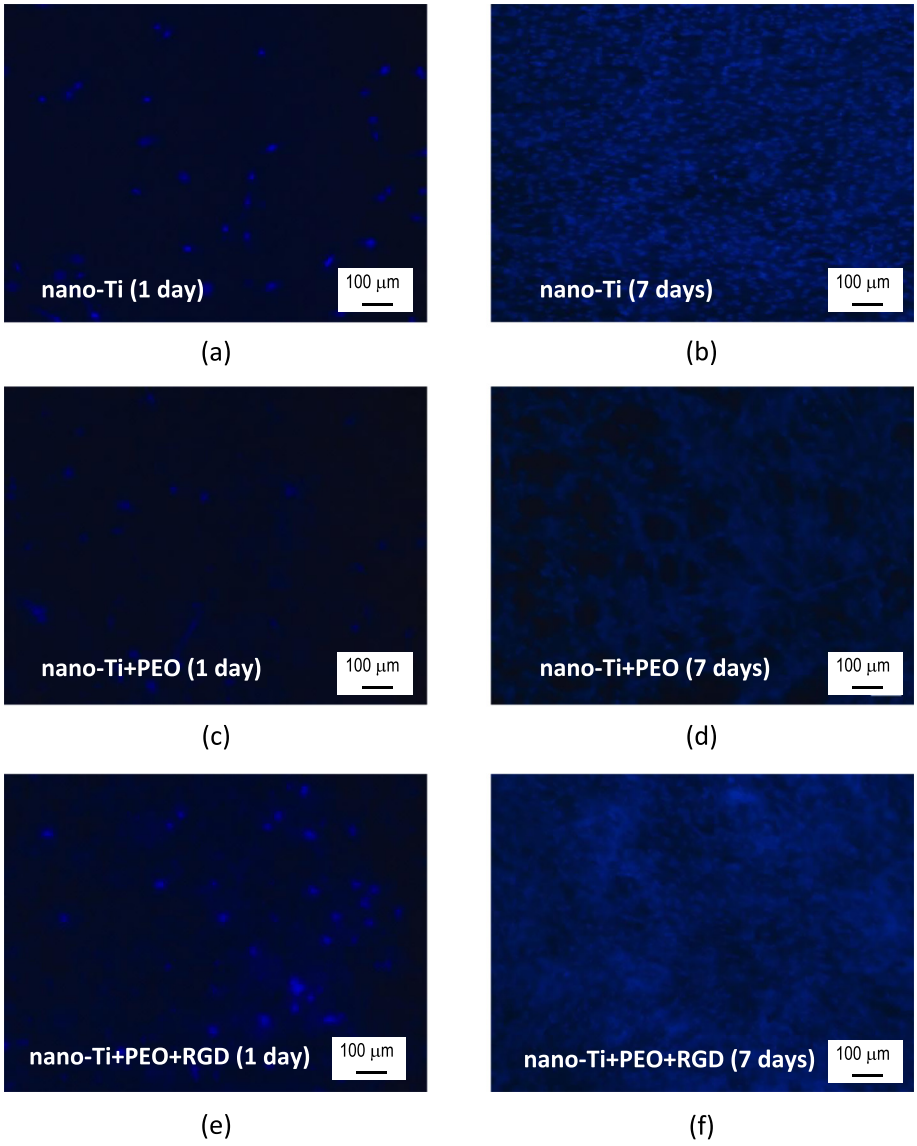

Fig. 13. Fluorescence microscope images of fibroblast cell nuclei after proliferation test for the nanostructured Ti samples: (a) nano-Ti, 1 day; (b) nano-Ti, 7 days; (c) nano-Ti + PEO, 1 day; (d) nano-Ti + PEO, 7 days; (e) nano-Ti + PEO + RGD, 1 day; (f) nano-Ti + PEO + RGD, 7 days.

surface; PEO coating on nano-Ti gives 43% increase in the number of cells compared to CG-Ti + PEO; the combination of PEO coating and RGD peptides on nano-Ti gives 45% increase in the number of cells compared to nano-Ti, and 66% compared to both uncoated and coated CG-Ti; this contributes to the development of a new generation of implants with advanced surface properties.

Acknowledgments

The authors are grateful to the support received through RFBR projects No. 17-03-01042 and 16-38-60062 and through the grant of Ministry of Education and Science of the Russian Federation No. 16.7268.2017/8.9. The structural studies of compounds **1–3** were performed in Collective Usage Centre “Agidel” at the Institute of Petrochemistry and Catalysis, RAS.

References

[1] M. Rehman, A. Madni, T.J. Webster, The era of biofunctional biomaterials in orthopedics: what does the future hold? Expert Rev. Med. Devices 15 (2018) 193–204.
[2] A.M. Khorasani, M. Goldberg, E.H. Doeven, G. Littlefair, Titanium in biomedical applications—properties and fabrication: a review, J. Biomater. Tissue Eng. 5 (2015) 593–619.
[3] M. Geetha, A.K. Singh, R. Asokamani, A.K. Gogia, Ti based biomaterials, the ultimate choice for orthopaedic implants – a review, Prog. Mater. Sci. 54 (2009) 397–425.
[4] R.Z. Valiev, Y. Estrin, Z. Horita, T.G. Langdon, M.J. Zehetbauer, Y.T. Zhu, Producing bulk ultrafine-grained materials by severe plastic deformation, JOM 58 (2006) 33–39.
[5] R.Z. Valiev, Superior strength in ultrafine-grained materials produced by SPD processing, Mater. Trans. 55 (2014) 13–18.
[6] R. Valiev, Nanostructuring of metals by severe plastic deformation for advanced properties, Nat. Mater. 3 (2004) 511.
[7] L. Mishnaevsky, E. Levashov, R.Z. Valiev, J. Segurado, I. Sabirov, N. Enikeev, S. Prokoshkin, A.V. Solov'yov, A. Korotitskiy, E. Gutmanas, I. Gotman, E. Rabkin, S. Psakh'e, L. Dluhoš, M. Seefeldt, A. Smolin, Nanostructured titanium-based materials for medical implants: modeling and development, Mater. Sci. Eng. R. Rep. 81 (2014) 1–19.
[8] A.V. Polyakov, L. Dluhoš, G.S. Dyakonov, G.I. Raab, R.Z. Valiev, Recent advances in processing and application of nanostructured titanium for dental implants, Adv. Eng. Mater. 17 (2015) 1869–1875.
[9] J.C.E. Odekerken, T.J.M. Welting, J.J.C. Arts, G.H.I.M. Walenkamp, P.J. Emans, Modern orthopaedic implant coatings — their pro's, con's and evaluation methods, in: M. Aliofkhazraei (Ed.), Modern Surface Engineering Treatments IntechOpen, New York, 2013, pp. 45–73.
[10] A.M. Greiner, A. Sales, H. Chen, S.A. Biela, D. Kaufmann, R. Kemkemer, Nano- and microstructured materials for in vitro studies of the physiology of vascular cells, Beilstein J. Nanotechnol. 7 (2016) 1620–1641.
[11] L. Bacakova, E. Filova, M. Parizek, T. Ruml, V. Svorcik, Modulation of cell adhesion,

proliferation and differentiation on materials designed for body implants, Biotechnol. Adv. 29 (2011) 739–767.
[12] F. Variola, F. Vetrone, L. Richert, P. Jedrzejowski, J.-H. Yi, S. Zalzal, S. Clair, A. Sarkissian, D.F. Perepichka, J.D. Wuest, F. Rosei, A. Nanci, Improving Biocompatibility of Implantable Metals by Nanoscale Modification of Surfaces: An Overview of Strategies, Fabrication Methods, and Challenges, Small, 5 (2009), pp. 996–1006.
[13] K. Anselme, M. Bigerelle, Role of materials surface topography on mammalian cell response, Int. Mater. Rev. 56 (2011) 243–266.
[14] F. Variola, J.H. Yi, L. Richert, J.D. Wuest, F. Rosei, A. Nanci, Tailoring the surface properties of Ti6Al4V by controlled chemical oxidation, Biomaterials 29 (2008) 1285–1298.
[15] G. Legeay, A. Coudreuse, F. Poncin-Epaillard, J.M. Herry, M.N. Bellon-Fontaine, Surface engineering and cell adhesion, J. Adhes. Sci. Technol. 24 (2010) 2301–2322.
[16] S. Bauer, P. Schmuki, K. von der Mark, J. Park, Engineering biocompatible implant surfaces, Prog. Mater. Sci. 58 (2013) 261–326.
[17] S.V. Dorozhkin, Calcium orthophosphate deposits: preparation, properties and biomedical applications, Mater. Sci. Eng. C Mater. Biol. Appl. 55 (2015) 272–326.
[18] F. Rupp, L. Liang, J. Geis-Gerstorfer, L. Scheideler, F. Hüttig, Surface characteristics of dental implants: a review, Dent. Mater. 34 (2018) 40–57.
[19] W.S.W. Harun, R.I.M. Asri, J. Alias, F.H. Zulkifli, K. Kadirgama, S.A.C. Ghani, J.H.M. Shariffuddin, A comprehensive review of hydroxyapatite-based coatings adhesion on metallic biomaterials, Ceram. Int. 44 (2018) 1250–1268.
[20] M.V. Diamanti, B. Del Curto, M. Pedeferri, Anodic oxidation of titanium: from technical aspects to biomedical applications, J. Appl. Biomater. Biomech. 9 (2011) 55–69.
[21] K. von der Mark, J. Park, Engineering biocompatible implant surfaces, Prog. Mater. Sci. 58 (2013) 327–381.
[22] S.R. Meyers, M.W. Grinstaff, Biocompatible and bioactive surface modifications for prolonged in vivo efficacy, Chem. Rev. 112 (2012) 1615–1632.
[23] A. Yerokhin, E.V. Parfenov, A. Matthews, In situ impedance spectroscopy of the plasma electrolytic oxidation process for deposition of Ca- and P-containing coatings on Ti, Surf. Coat. Technol. 301 (2016) 54–62.
[24] E. Matykina, P. Skeldon, G.E. Thompson, Fundamental and practical evaluation of plasma electrolytic oxidation coatings of titanium, Surf. Eng. 23 (2013) 412–418.
[25] S.A. Yavari, B.S. Necula, L.E. Fratila-Apachitei, J. Duszczyk, I. Apachitei, Biofunctional surfaces by plasma electrolytic oxidation on titanium biomedical alloys, Surf. Eng. 32 (2016) 411–417.
[26] Y. Wang, H. Yu, C. Chen, Z. Zhao, Review of the biocompatibility of micro-arc oxidation coated titanium alloys, Mater. Des. 85 (2015) 640–652.
[27] E.V. Parfenov, A. Yerokhin, R.R. Nevyantseva, M.V. Gorbatkov, C.J. Liang, A. Matthews, Towards smart electrolytic plasma technologies: an overview of methodological approaches to process modelling, Surf. Coat. Technol. 269 (2015) 2–22.
[28] H. Sharifi, M. Aliofkhazraei, G.B. Darband, S. Shrestha, A review on adhesion strength of peo coatings by scratch test method, Surf. Rev. Lett. 25 (2018).
[29] W.K. Yeung, G.C. Reilly, A. Matthews, A. Yerokhin, In vitro biological response of plasma electrolytically oxidized and plasma-sprayed hydroxyapatite coatings on Ti-6Al-4V alloy, J Biomed Mater Res B Appl Biomater 101 (2013) 939–949.
[30] S. Gowtham, T. Arunnellaiappan, N. Rameshbabu, An investigation on pulsed DC plasma electrolytic oxidation of cp-Ti and its corrosion behaviour in simulated body fluid, Surf. Coat. Technol. 301 (2016) 63–73.
[31] A. Kazek-Kesik, M. Krok-Borkowicz, E. Pamula, W. Simka, Electrochemical and biological characterization of coatings formed on Ti-15Mo alloy by plasma electrolytic oxidation, Mater. Sci. Eng. C Mater. Biol. Appl. 43 (2014) 172–181.
[32] S.V. Gnedenkov, Y.P. Sharkeev, S.L. Sinebryukhov, O.A. Khrisanfova, E.V. Legostaeva, A.G. Zavidnaya, A.V. Puz', I.A. Khlusov, D.P. Opra, Functional coatings formed on the titanium and magnesium alloys as implant materials by plasma electrolytic oxidation technology: fundamental principles and synthesis conditions, Corros. Rev. 34 (2016).
[33] A. Santos-Coquillat, E. Martínez-Campos, M. Mohedano, R. Martínez-Corriá, V. Ramos, R. Arrabal, E. Matykina, In vitro and in vivo evaluation of PEO-modified titanium for bone implant applications, Surf. Coat. Technol. 347 (2018) 358–368.
[34] L. Xu, K. Zhang, C. Wu, X. Lei, J. Ding, X. Shi, C. Liu, Micro-arc oxidation enhances the blood compatibility of ultrafine-grained pure titanium, Materials 10 (2017) (Basel).
[35] F. Reshadi, G. Faraji, M. Baniassadi, M. Tajeddini, Surface modification of severe plastically deformed ultrafine grained pure titanium by plasma electrolytic oxidation, Surf. Coat. Technol. 316 (2017) 113–121.
[36] A. Alsaran, G. Purcek, I. Hacisalihoglu, Y. Vangolu, Ö. Bayrak, I. Karaman, A. Celik, Hydroxyapatite production on ultrafine-grained pure titanium by micro-arc oxidation and hydrothermal treatment, Surf. Coat. Technol. 205 (2011) S537–S542.
[37] E. Ruoslahti, RGD and other recognition sequences for integrins, Annu. Rev. Cell Dev. Biol. (1996) 697–715.
[38] J. Goura, V. Chandrasekhar, Molecular metal phosphonates, Chem. Rev. 115 (2015) 6854–6965.
[39] B.M. Silverman, K.A. Wieghaus, J. Schwartz, Comparative properties of siloxane vs phosphonate monolayers on a key titanium alloy, Langmuir 21 (2005) 225–228.
[40] J. Beuvelot, D. Portet, G. Lecollinet, M.F. Moreau, M.F. Baslé, D. Chappard, H. Libouban, In vitro kinetic study of growth and mineralization of osteoblast-like cells (Saos-2) on titanium surface coated with a RGD functionalized bisphosphonate, J Biomed Mater Res B Appl Biomater 90 (B) (2009) 873–881.
[41] Y. Su, C. Luo, Z. Zhang, H. Hermawan, D. Zhu, J. Huang, Y. Liang, G. Li, L. Ren, Bioinspired surface functionalization of metallic biomaterials, J. Mech. Behav. Biomed. Mater. 77 (2018) 90–105.
[42] S. Wu, X. Liu, K.W.K. Yeung, C. Liu, X. Yang, Biomimetic porous scaffolds for bone tissue engineering, Mater. Sci. Eng. R. Rep. 80 (2014) 1–36.
[43] B. Thierry, F.M. Winnik, Y. Merhi, H.J. Griesser, M. Tabrizian, Biomimetic hemocompatible coatings through immobilization of hyaluronan derivatives on metal surfaces, Langmuir 24 (2008) 11834–11841.
[44] T.S. Zaporozhets, A.V. Puz', S.L. Sinebryukhov, S.V. Gnedenkov, T.P. Smolina, N.N. Besednova, Biocompatibility of modified osteoinductive calcium-phosphate coatings of metal implants, Bull. Exp. Biol. Med. 162 (2017) 366–369.
[45] M.P. Neupane, I.S. Park, M.H. Lee, Surface characterization and corrosion behavior of micro-arc oxidized Ti surface modified with hydrothermal treatment and chitosan coating, Thin Solid Films 550 (2014) 268–271.
[46] A. Kazek-Kęsik, J. Jaworska, M. Krok-Borkowicz, M. Gołda-Cepa, M. Pastusiak, M. Brzychczy-Włoch, E. Pamuła, A. Kotarba, W. Simka, Hybrid oxide-polymer layer formed on Ti-15Mo alloy surface enhancing antibacterial and osseointegration functions, Surf. Coat. Technol. 302 (2016) 158–165.
[47] L. Pezzato, P. Cerchier, K. Brunelli, A. Bartolozzi, R. Bertani, M. Dabalà, Plasma electrolytic oxidation coatings with fungicidal properties, Surf. Eng. (2018) 1–9, https://doi.org/10.1080/02670844.2018.1441659.
[48] G.S. Dyakonov, E. Zemtsova, S. Mironov, I.P. Semenova, R.Z. Valiev, S.L. Semiatin, An EBSD investigation of ultrafine-grain titanium for biomedical applications, Mater. Sci. Eng. A 648 (2015) 305–310.
[49] R. Kovács, A. Grün, O. Németh, S. Garadnay, I. Greiner, G. Keglevich, The synthesis of pamidronic derivatives in different solvents: an optimization and a mechanistic study, Heteroat. Chem. 25 (2014) 186–193.
[50] P.C. Tyler, R.N. Young, G.A. Rodan, R. Ruel, Prostaglandin Analog for Treating Osteoporosis, US Patent 5, 409, 911, (1995).
[51] L. Keller, W.A. Dollase, X-ray determination of crystalline hydroxyapatite to amorphous calcium- phosphate ratio in plasma sprayed coatings, J. Biomed. Mater. Res. 49 (2000) 244–249.
[52] F.H. Chung, Quantitative interpretation of X-ray diffraction patterns of mixtures. I. Matrix-flushing method for quantitative multicomponent analysis, J. Appl. Crystallogr. 7 (1974) 513–519.
[53] J.R. Scully, Polarization resistance method for determination of instantaneous corrosion rates, Corrosion 56 (2000) 199–217.
[54] E. Barsukov, J.R. Macdonald, Impedance Spectroscopy: Theory, Experiment, and Applications, 2nd ed., John Willey & Sons, Inc., Hoboken, 2005.
[55] M.J. Dalby, S.J. Yarwood, M.O. Riehle, H.J.H. Johnstone, S. Affrossman, A.S.G. Curtis, Increasing fibroblast response to materials using nanotopography: morphological and genetic measurements of cell response to 13-nm-high polymer demixed Islands, Exp. Cell Res. 276 (2002) 1–9.
[56] B. Grossner-Schreiber, M. Herzog, J. Hedderich, A. Duck, M. Hannig, M. Griepentrog, Focal adhesion contact formation by fibroblasts cultured on surface-modified dental implants: an in vitro study, Clin. Oral Implants Res. 17 (2006) 736–745.
[57] L. Richert, F. Vetrone, J.-H. Yi, S.F. Zalzal, J.D. Wuest, F. Rosei, A. Nanci, Surface nanopatterning to control cell growth, Adv. Mater. 20 (2008) 1488–1492.
[58] C. Zhou, F. Lei, J. Chodosh, E.I. Paschalis, The role of titanium surface microtopography on adhesion, proliferation, transformation, and matrix deposition of corneal cells, Invest. Ophthalmol. Vis. Sci. 57 (2016) 1927–1938.
[59] M. Chávez-Díaz, M. Escudero-Rincón, E. Arce-Estrada, R. Cabrera-Sierra, Effect of the heat-treated Ti6Al4V alloy on the fibroblastic cell response, Materials 11 (2018) 21.
[60] C.C. Koch, T.G. Langdon, E.J. Lavernia, Bulk nanostructured materials, Metall. Mater. Trans. A 48 (2017) 5181–5199.
[61] D.M. Brunette, Titanium in Medicine: Material Science, Surface Science, Engineering, Biological Responses, and Medical Applications, Springer, Berlin; New York, 2001.
[62] Y. Estrin, A. Vinogradov, Fatigue behaviour of light alloys with ultrafine grain structure produced by severe plastic deformation: an overview, Int. J. Fatigue 32 (2010) 898–907.
[63] A. Nominé, S.C. Troughton, A.V. Nominé, G. Henrion, T.W. Clyne, High speed video evidence for localised discharge cascades during plasma electrolytic oxidation, Surf. Coat. Technol. 269 (2015) 125–130.
[64] E. Matykina, R. Arrabal, R.Z. Valiev, J.M. Molina-Aldareguia, P. Belov, I. Sabirov, Electrochemical anisotropy of nanostructured titanium for biomedical implants, Electrochim. Acta 176 (2015) 1221–1232.
[65] K.D. Ralston, N. Birbilis, Effect of grain size on corrosion: a review, Corrosion 66 (2010) (075005-075005-075013).
[66] H. Miyamoto, Corrosion of ultrafine grained materials by severe plastic deformation, an overview, materials transactions, 57 (2016) 559–572.
[67] M. Roknian, A. Fattah-alhosseini, S.O. Gashti, Plasma electrolytic oxidation coatings on pure Ti substrate: effects of Na3PO4 concentration on morphology and corrosion behavior of coatings in Ringer's physiological solution, J. Mater. Eng. Perform. 27 (2018) 1343–1351.
[68] K.-H. Kim, R. Narayanan, T.R. Rautray, Surface Modification of Titanium for Biomaterial Applications, Nova Science Publishers, New York, 2010.
[69] R.Z. LeGeros, Calcium phosphate-based osteoinductive materials, Chem. Rev. 108 (2008) 4742–4753.
[70] F.H. van Heuvein, Analysis of nonexponential transient response due to a constant-phase element, J. Electrochem. Soc. 141 (1994) 3423–3428.
[71] D. Dzhurinskiy, Y. Gao, W.K. Yeung, E. Strumban, V. Leshchinsky, P.J. Chu, A. Matthews, A. Yerokhin, R.G. Maev, Characterization and corrosion evaluation of TiO2:n-HA coatings on titanium alloy formed by plasma electrolytic oxidation, Surf. Coat. Technol. 269 (2015) 258–265.
[72] S.V. Gnedenkov, S.L. Sinebryukhov, A.V. Puz, V.S. Egorkin, R.E. Kostiv, In vivo study of osteogenerating properties of calcium-phosphate coating on titanium alloy

Ti-6Al-4V, Bio-Med. Mater. Eng. 27 (2016) 551–560.
[73] S. Hariprasad, M. Ashfaq, T. Arunnellaiappan, M. Harilal, N. Rameshbabu, Role of electrolyte additives on in-vitro corrosion behavior of DC plasma electrolytic oxidization coatings formed on Cp-Ti, Surf. Coat. Technol. 292 (2016) 20–29.
[74] M. Köunönen, M. Hormia, J. Kivilahti, J. Hautaniemi, I. Thesleff, Effect of surface processing on the attachment, orientation, and proliferation of human gingival fibroblasts on titanium, J. Biomed. Mater. Res. 26 (1992) 1325–1341.
[75] K.R. Shin, Y.S. Kim, J.H. Jeong, Y.G. Ko, D.H. Shin, Pore size effect on cell response via plasma electrolytic oxidation, Surf. Eng. 32 (2016) 418–422.
[76] P.-H. Chua, K.-G. Neoh, E.-T. Kang, W. Wang, Surface functionalization of titanium with hyaluronic acid/chitosan polyelectrolyte multilayers and RGD for promoting osteoblast functions and inhibiting bacterial adhesion, Biomaterials 29 (2008) 1412–1421.
[77] A.G. Secchi, V. Grigoriou, I.M. Shapiro, E.A. Cavalcanti-Adam, R.J. Composto, P. Ducheyne, C.S. Adams, RGDS peptides immobilized on titanium alloy stimulate bone cell attachment, differentiation and confer resistance to apoptosis, J. Biomed. Mater. Res. A 83 (2007) 577–584.
[78] Z. Shi, K.G. Neoh, E.T. Kang, C. Poh, W. Wang, Bacterial adhesion and osteoblast function on titanium with surface-grafted chitosan and immobilized RGD peptide, J. Biomed. Mater. Res. A 86 (2008) 865–872.